n-Beam Lattice Images. IV. Computed Two-Dimensional Images*

By M. A. O'Keefe

CSIRO Division of Tribophysics, University of Melbourne, Parkville, Victoria, 3052, Australia

The contrast in electron-microscope lattice images of crystals oriented with a zone axis parallel to the incident electron beam has been computed for several complex oxides with large unit cells. The effects of changes in crystal thickness, image defocus, objective aperture size (up to 100 contributing diffracted beams) and spherical aberration are considered, and it is shown that, under certain conditions, the appearance of the image resembles that of the crystal structure. The bounds of applicability of the simple charge-density approximation are investigated.

1. Introduction

The technique of lattice imaging has recently been applied to the study of complex oxides with large unit cells, and there is good experimental evidence that in favourable circumstances direct correlations between image contrast and structural features are justified (Allpress, Sanders & Wadsley, 1969; Allpress, 1969a). In part I (Allpress, Hewat, Moodie & Sanders, 1972) of this series, the relatively simple case of an image formed using diffracted beams from a systematic set (00l, $|l| \leq 5$) was examined in detail. For this case of a one-dimensional image, it was shown that agreement between experimental and computed image contrast could be realized, and conditions were outlined under which direct information about structure might be obtained.

From an experimental point of view, images formed from a two-dimensional set of diffracted beams (*e.g.*, h0l) have proved to be of great interest and value (Allpress, 1969b, 1970; Van Landuyt, Vochten & Amelinckx, 1970; Iijima, 1971, 1973; Cowley & Iijima, 1972a; Hutchison & Anderson, 1972; Anderson, Browne & Hutchison, 1972a,b). However, the choice of parameters such as crystal thickness and image defocus appears to be more critical in this situation than for the simpler one-dimensional images (Cowley & Iijima, 1972b). In order to establish the conditions under which two-dimensional images of these oxides can be simply related to their structures, the methods of computing image contrast, which were described in detail in part II (Lynch & O'Keefe, 1972) of this series of publications, have now been extended to the case when n beams from a h0l set contribute to the lattice image.

Preliminary comparisons with existing experimental data are very encouraging, and will be discussed in more detail elsewhere (Iijima & O'Keefe, 1973).

2. The calculations

The computation of image contrast can be achieved by several more or less approximate methods. The most accurate (and time consuming) of these involves the inverse Fourier transformation of the amplitudes and phases of the diffracted beams, which are themselves computed using a multislice procedure. This method is described in § 2.1 and the computed images are referred to subsequently as n-beam lattice images.

A second, and much simpler procedure, assumes that the crystal can be regarded as a thin phase grating, and in these circumstances, the contrast in the slightly underfocused image represents the projected charge distribution in the crystal (Cowley & Moodie, 1960). This approximation is dealt with in § 2.2, and the resultant images are referred to as n-coefficient projected charge density (n-PCD) images.

2.1 n-Beam lattice image contrast

2.1.1 The diffracted beams

Multislice calculations with 435 diffracted beams were carried out for each structure as described in part II, using scattering factors for neutral atoms, an overall isotropic temperature factor of 3×10^{-3} nm², and an incident electron energy of 100 keV. In each case, the incident electron beam was set parallel with the crystal b axis and the h0l diffracted beam amplitudes and phases were recorded as a function of crystal thickness in steps of 1·0 nm.

2.1.2 The n-beam lattice image

The complex wave functions of the diffracted beams at the required crystal thickness were inverse Fourier transformed to give two-dimensional images by the use of a two-dimensional form of the transformation described in part II. [It should be noted that both or either of the scattering and imaging calculations can be carried out in the one-dimensional or two-dimensional form. In parts I and II, a one-dimensional imaging approximation was used since the scattering calculations (both one- and two-dimensional) had been carried out with the crystal tilted into a systematic orientation.]

The character of the image is a function of the thickness, H, the defect of focus, ε, the number of beams over which the summation was carried out, n, and the magnitude of the spherical-aberration coefficient, C_s.

Transforming the propagated diffracted beams into real space gives the wave function at the image plane as:

$$\psi_{H,\varepsilon}(x,z) = \mathscr{F}^{-1}\{U_H(h,l) \cdot P_\varepsilon(h,l)\} \qquad (1)$$

and intensity as:

$$I(x,z) = \psi(x,z) \cdot \psi^*(x,z)$$

where $\mathscr{F}^{-1}$ signifies the inverse Fourier transformation, $U_H(h,l)$ is the amplitude and phase of the (h,l)th diffracted beam from a crystal of thickness H and, for a defect of focus ε, the propagator is:

$$P_\varepsilon(h,l) = \exp\{2\pi i \zeta(h,l)[\varepsilon - \lambda C_s \zeta(h,l)]\} \qquad (2)$$

where $-\lambda C_s \zeta(h,l)$ is the additional overfocus of the (h,l)th beam due to spherical aberration and $\zeta(h,l)$ is its excitation error (negative outside the Ewald sphere).

Substituting for P in equation (1), the image wave function for an apertured image becomes:

$$\psi_{H,\varepsilon,n,C_s}(x,z) = \sum_h \sum_l U_H(h,l) \cdot \exp[2\pi i\{\zeta(h,l)$$

$$\times [\varepsilon - \lambda C_s \zeta(h,l)] - \left(\frac{hx}{a} + \frac{lz}{c}\right)\}] \qquad (3)$$

where the summations are carried out over only those n beams passing through the aperture. For images of any particular structure, calculated for the case of a circular aperture centred on the 000 beam, n is a function only of the radius, R, of the aperture, where R, measured in terms of the spacing of the 00l reflexions becomes R^*. Thus, the $h0l$ beams which pass through an aperture of 00l radius R^* are those which satisfy the relation

$$(R^*c^*)^2 \geq (ha^*)^2 + 2ha^*lc^* \cos \beta^* + (lc^*)^2 \qquad (4)$$

and the resolution attained in the resultant n-beam image is $d_R = (R^*c^*)^{-1}$.

The calculated images were displayed in the form of half-tone printouts, of 3×3 unit cells in area, produced by the lineprinter (Head, 1967) and required 3 min of CDC 3200 computer time for the computation of each image, compared with 16 sec for a one-dimensional image.

2.2 The projected charge density (n-PCD) approximation

If we assume that the crystal is sufficiently thin to behave as a phase grating, then the image can be obtained directly from the kinematic structure amplitudes (part II). Since no multislice computation is involved, the procedure is much faster than that required to obtain the true n-beam lattice image. This useful approximation was proposed by Cowley &

Moodie (1960), and was demonstrated for one-dimensional lattice images in parts I, II and III (Anstis, Lynch, Moodie & O'Keefe, 1973) of this series. It states that for crystals thin enough to satisfy the Single-Slice or Phase-Grating Approximation (Cowley & Moodie, 1957a, 1962), imaged with small defects of focus and effectively infinite aperture,[†] the crystal lattice image intensity will be given by

$$I(x,z) = 1 - \frac{\sigma\lambda\varepsilon}{2\pi} \cdot \nabla^2\varphi_p(x,z) \qquad (5)$$

where σ is the interaction parameter (Cowley & Moodie, 1960) and the n-coefficient projected charge density is:

$$\varrho_p(x,z) \propto \nabla^2\varphi_p(x,z)$$

$$= -16\pi^2 H \sum_h \sum_l \exp\left\{2\pi i\left(\frac{hx}{a} + \frac{lz}{c}\right)\right\} \cdot V(h,l) \cdot s^2(h,l) \,(6)$$

where for the (h,l)th beam, Bragg angle $\theta(h,l)$, we have $s(h,l) = \sin \theta(h,l)/\lambda$ and $V(h,l)$ is its structure amplitude in volts.

The approximation fails when the second term in equation (5) approaches unity. For a given incident electron energy (λ and σ constant), this will occur for large values of defect of focus, ε, or crystal thickness, H; similarly, increasing the resolution (increasing n) will increase the excursions in value of $\nabla^2\varphi_p$ and lead to failure. Thus, as resolution increases the approximation requires that the product ε. H be decreased if the n-PCD image is to correspond with the n-beam lattice image.

Another requirement of this approximation is that the defect of focus, ε, be small (Cowley & Moodie, 1960) so that

$$\exp\{-i\pi|\varepsilon|\lambda(R^*c^*)^2\} \simeq 1 - i\pi|\varepsilon|\lambda(R^*c^*)^2.$$

This will hold when

$$\pi|\varepsilon|\lambda(R^*c^*)^2 \ll \pi. \qquad (7)$$

Thus, at a given resolution, the approximation places an upper limit on ε such that $|\varepsilon| \ll d_R^2/\lambda$.

n-PCD images were calculated using the summation over n coefficients for comparison with n-beam lattice images in order to determine the limits of crystal thickness and defect of focus within which the approximation holds.

3. The structures

The calculations described above were carried out for crystals of $W_4Nb_{26}O_{77}$, $TiNb_{24}O_{62}$ and $Ti_2Nb_{10}O_{29}$, the structures of which have been determined by X-ray methods (Table 1). Unit cells of these structures are made up of blocks of corner-sharing MO_6 octahedra

---

† The expression for finite aperture is given in part II and Moodie (1973) and will be investigated in detail in part V of this series.
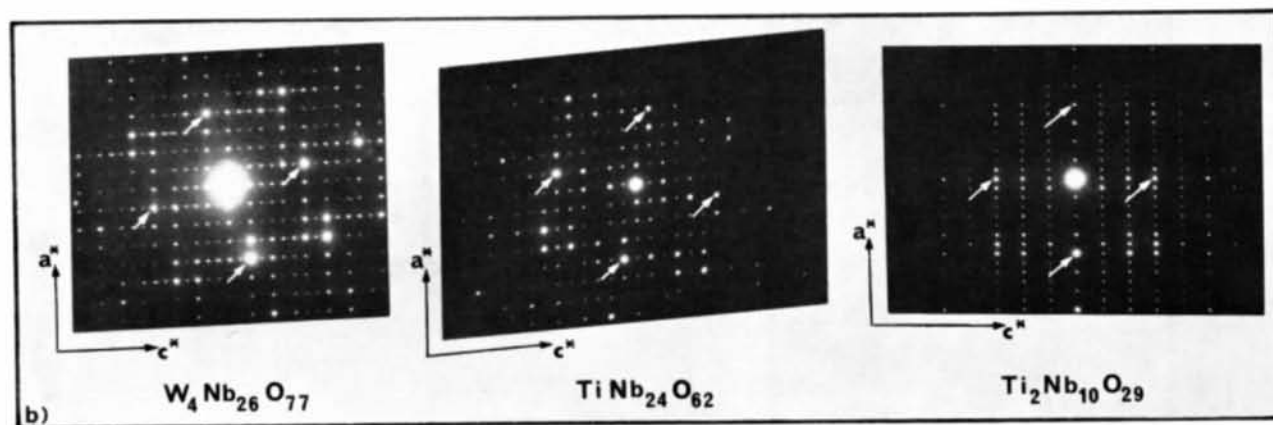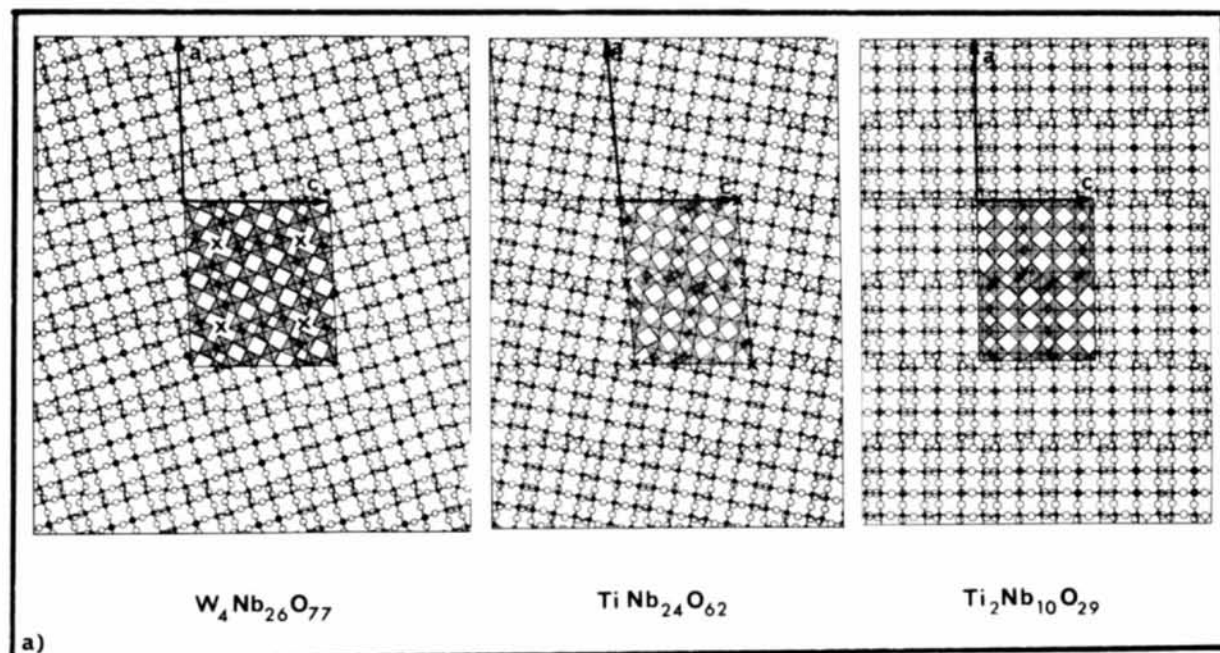
a)

W₄Nb₂₆O₇₇   TiNb₂₄O₆₂   Ti₂Nb₁₀O₂₉

b)

W₄Nb₂₆O₇₇   TiNb₂₄O₆₂   Ti₂Nb₁₀O₂₉

Fig. 1. (a) Models of the three structures viewed down [010]. Each covers an area of 3×3 unit cells. In each case, one unit cell is drawn in the form of blocks of MO_6 octahedra with the positions of tetrahedrally coordinated metal atoms marked X, and the empty tunnels parallel to [010] can easily be seen. The remainders of the areas show metal atom positions as solid black circles and those of the oxygen atoms as larger open circles. Unit cell axes are indicated. (b) Electron diffraction patterns (courtesy J. G. Allpress) from the three structures showing the number of reflexions included in the 435-beam dynamical scattering calculations. The sublattice reflexions referred to in the text are indicated by arrows. The a^* and c^* directions are indicated.

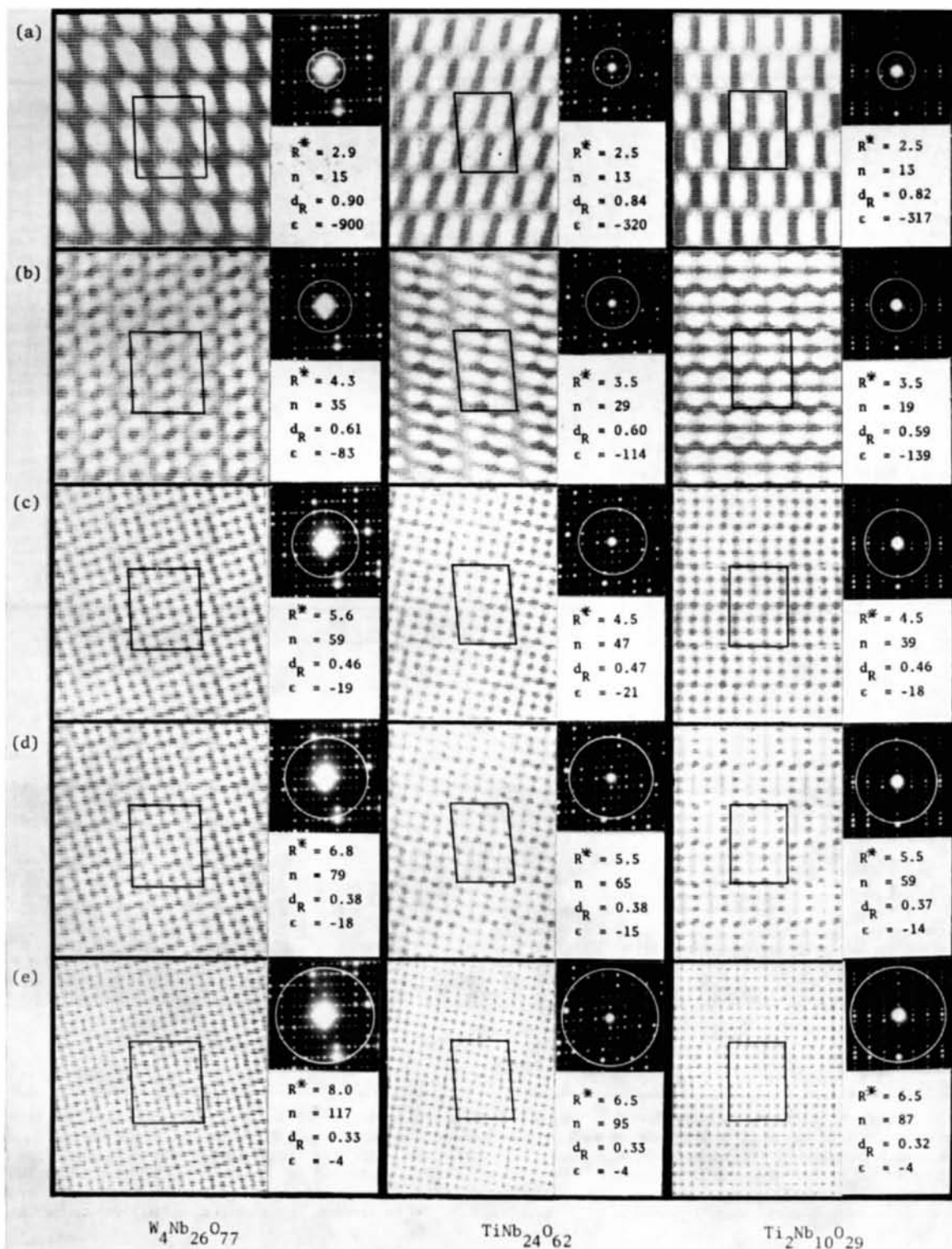$W_4Nb_{26}O_{77}$ $TiNb_{24}O_{62}$ $Ti_2Nb_{10}O_{29}$

Fig. 3. *n*-PCD images of the three structures for crystals 5 nm in thickness, showing the effect of increasing the number of Fourier coefficients (*n*) on the image resolution. The images in row (*c*) are most readily interpreted in terms of structure. The corresponding experimental situations are illustrated by the diffraction patterns on the right of the images, in which the white circles mark the size of the objective aperture. R^* is the aperture radius in 00*l* units, d_R the image resolution in nm, and ε the defocus in nm.
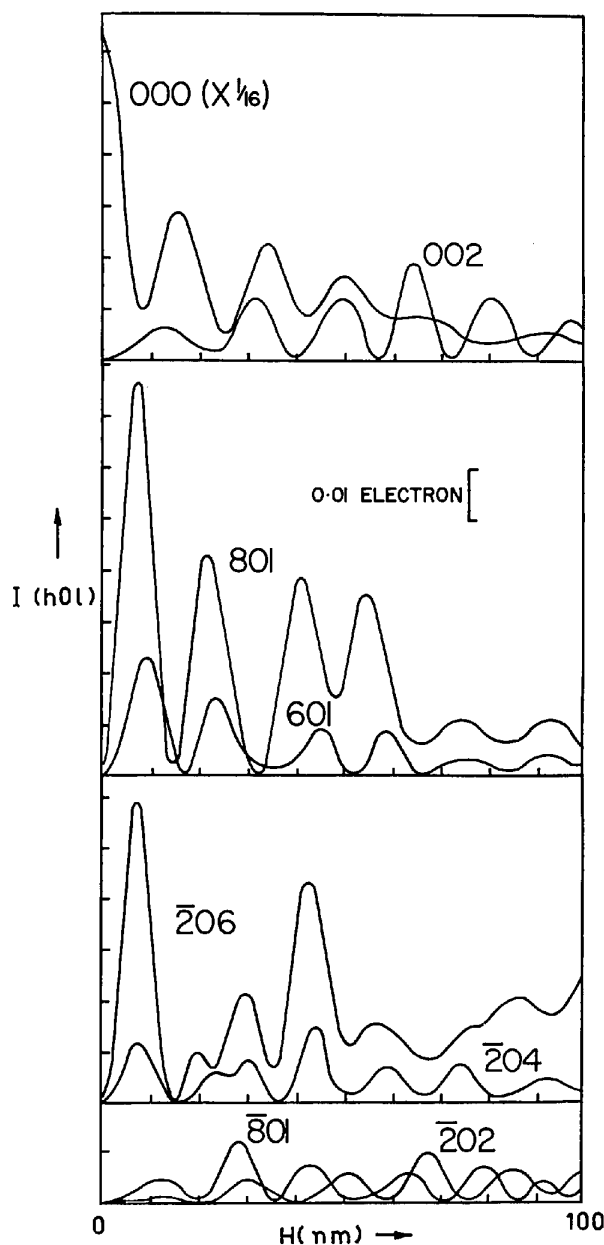
Fig. 2. Calculated intensities $I(h0l)$ for some diffracted beams as a function of crystal thickness, H, for $TiNb_{24}O_{62}$. Quasi-periods of the beams range from 15 to 20 nm.

(M = metal); these blocks join by sharing octahedral edges and, in projection down the short b axis, can be represented as in Fig. 1(a).

In the $W_4Nb_{26}O_{77}$ and $TiNb_{24}O_{62}$ structures, joining by block overlap creates tetrahedral sites near the corners of some of the blocks and these are filled with metal atoms. In Fig. 1, the areas shown cover 3×3 unit cells (the same area as displayed in the computed images) and two representations of the structures are employed in each case; one unit cell is shown as made up of MO_6 octahedra in projection with the positions of tetrahedrally coordinated metal atoms marked with crosses, while over the remainder of the area atom positions appear as solid black circles (metal atoms) and larger open circles (oxygens).

4. Results

4.1 Diffracted beam intensities

The 435-beam dynamical scattering (multislice) calculations were carried out using the $h0l$ zone reflexions that are shown in the experimental diffraction patterns of Fig. 1(b). The multislice calculations exhibited much more dynamic character than those carried out with the crystal tilted into a systematic orientation as described in part II. This was because of the larger number of beams with small excitation errors and resulted in two main effects.

The first effect was increased weak-beam absorption (as defined in part II) which occurred since more energy was 'lost' to outer beams not included in the calculation. This led, for unit electron-intensity input, to total electron intensities of approximately 0·9 and 0·7 at crystal thicknesses of 10 and 30 nm respectively. Such low normalizations, while disturbing in the context of diffracted-beam intensities for comparison with experiment, do not significantly alter the relative values of the diffracted-beam amplitudes and phases to be used for imaging. In part II of this series, it was shown for the systematics case that images calculated for a crystal 30 nm thick were very similar when the results of either a 435- or 105-beam multislice calculation were used, even though the normalizations were respectively 0·86 and 0·44.

The second effect resulting from the increased coupling in a zone-axis configuration compared with that in a systematics one is a reduction in the quasi-

Table 1. The three structures used in the calculations

System	$W_4Nb_{29}O_{77}$ Monoclinic ($C2$)	$TiNb_{24}O_{62}$ Monoclinic ($C2$)	$Ti_2Nb_{10}O_{29}$ Orthorhombic ($Amma$)
a (nm)	2·974	2·978	2·850
b (nm)	0·3824	0·3821	0·3805
c (nm)	2·597	2·112	2·051
β (rad)	1·611	1·656	1·571
Reference	Andersson, Mumme & Wadsley (1966)	Roth & Wadsley (1965)	Wadsley (1961)

period (part III) of the diffracted beam intensities. Plots of beam intensity, $I(h0l)$, against crystal thickness, H, for some of the more intense beams (Fig. 2) show that, while there is no true periodicity, the intensities of the stronger beams tend to fall to zero and recur every 15–20 nm.

4.2 Images near projected-charge-density conditions

The four parameters investigated for thin crystals at small negative defect of focus were:

(i) the number of beams, n, contributing to the image;
(ii) the crystal thickness, H;
(iii) the defect of focus, ε;
(iv) the spherical-aberration coefficient, C_s, in the microscope lens system.

The bounds of the values of the four parameters were restricted so that n and C_s were near commonly encountered experimental values, and H and ε were near values for which the n-PCD approximation might reasonably be expected to apply (*i.e.* thin crystals at small negative defects of focus).

4.2.1 Number of beams

The effect of varying n on the lattice image of a thin crystal at small negative defocus was investigated by examining n-PCD images evaluated using equations (5) and (6). The white circles on the diffraction patterns of Fig. 3 indicate the number of structure amplitudes included in the calculation of the corresponding charge-density image. In order to obtain the maximum contrast in each image, the magnitude of the negative defect of focus was in each case chosen to be as large as possible consistent with the requirement that the intensity $I(x,z)$ of equation (5) be positive for all x,z. The effect of negative defocus is to produce an image which is dark in areas of high negative charge density.

For the smallest aperture [Fig. 3(a)], each structure imaged as thick black lines in areas corresponding to overlap of blocks of MO_6 octahedra, surrounding white patches centred on each block. The white patches may be considered as an association of the groups of hollow tunnels which exist in the structures viewed at low resolution. These tunnels consist of the spaces between the octahedra forming 4×3 blocks in $TiNb_{24}O_{62}$ and $Ti_2Nb_{10}O_{29}$ and alternating 4×4 and 3×4 blocks in $W_4Nb_{26}O_{77}$ [Fig. 1(a)].

With the aperture enlarged to give a resolution of $d_R \simeq 0.6$ nm [Fig. 3(b)], the groups of 2×3 tunnels in the 3×4 blocks appear as two white dots while the 3×3 groups of tunnels in $W_4Nb_{26}O_{77}$ image as four white dots surrounding a central black dot which is sited on a tunnel position.

When the aperture is just large enough to include the strong structure amplitudes which lie inside the stronger sublattice reflexions [arrowed in Fig. 1(b)], the patterns of white dots in the three n-PCD images [Fig. 3(c)] show a one-to-one correspondence with the empty tunnels in the structures, except that additional

(weaker) white spots appear in the positions of the tetrahedrally coordinated metal atoms in $W_4Nb_{26}O_{77}$ and $TiNb_{24}O_{62}$.

This pattern of white spots remains [Fig. 3(d)] as the aperture is widened so that the sublattice structure amplitudes are just excluded, but in the case of $TiNb_{24}O_{62}$ and $Ti_2Nb_{10}O_{29}$, the black dots which correspond to both individual and unresolved overlapping octahedra change intensity, the overlapping octahedra becoming darker than those in the interiors of blocks.

The sublattice structure amplitudes correspond to a resolution of approximately 0.38 nm (the length of an octahedron body-diagonal). When these are included in the projected-charge-density summation [Fig. 3(e)], the overlapping octahedra are resolved and black dots appear near the centres of all octahedra and at the positions of the tetrahedrally coordinated metal atoms. At this resolution, the proliferation of detail makes interpretation of the images more difficult than at lower resolutions where the sublattice structure amplitudes are excluded.

4.2.2 Crystal thickness

Equations (5) and (6) show that contrast in an n-PCD image is proportional to both ε and H. Thus, the n-PCD approximation predicts that an image will remain unaltered as the crystal thickness is increased, so long as the product $\varepsilon.H$ remains constant. However, with increasing crystal thickness, the phase-grating approximation becomes less applicable (Cowley & Moodie, 1962) and, hence, we may expect that the n-PCD image will become less and less representative of the true n-beam lattice image. Similarly, if the defocus ε is altered so that $|\varepsilon|$ is no longer small compared to d_R^2/λ [equation (7)], the n-PCD images will not correspond to true n-beam lattice images.

Both these effects appeared when n-beam lattice images were calculated for $W_4Nb_{26}O_{77}$ with the same values of n, H and ε as were used in the n-PCD images of Fig. 3. The first column of Fig. 4 shows $W_4Nb_{26}O_{77}$ n-PCD images for the five apertures of Fig. 3, the second column shows the equivalent n-beam lattice images, while the next two columns contain respectively n-beam lattice images calculated at twice the crystal thickness ($H = 10$ nm) and half the original ε, and three times the crystal thickness ($H = 15$ nm) and one third the original ε.

For the images at 0.9 nm resolution [Fig. 4(a)], the defects of focus are of greater magnitude than the value of d_R^2/λ (Table 2) so that the n-beam images do not match that calculated using the n-PCD approximation. Similarly, breakdown due to excessive defocus occurs for the n-PCD image of Fig. 4(b) where $H = 5$ nm and $R^* = 4.3$ since $d_R^2/\lambda = 100$ nm and $\varepsilon = -83$ nm.

The higher-resolution images in Fig. 4(c)–(e) satisfy the maximum-defocus condition and illustrate the failure of the n-PCD approximation with increasing crystal thickness. For $H = 5$ nm, the match between the $R^* = 5.6$ n-beam image and the equivalent n-PCD

image is extremely good [Fig. 4(c)], the major difference being the larger white spots in the n-beam image. At H= 10 nm, the white spots appear near the correct posi-tions and areas of block overlap are dark, but the match with the n-PCD image is poor. At H=15 nm the contrast in the n-beam image is the inverse of that

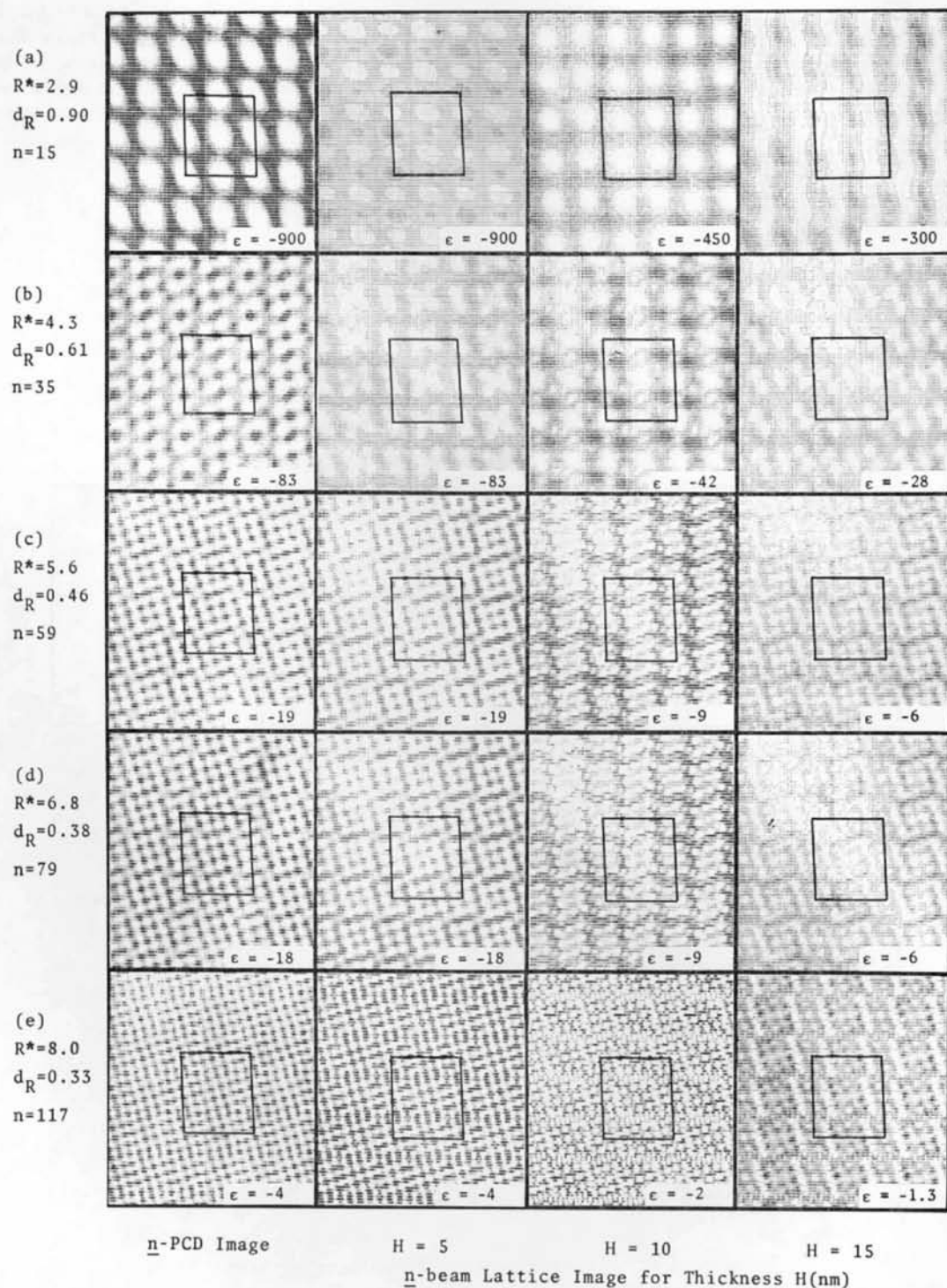

Fig. 4. Comparison of $W_4Nb_{26}O_{77}$ n-PCD images (left column) with n-beam lattice images of $W_4Nb_{26}O_{77}$ (remaining three columns) calculated for increasing crystal thickness H (nm), and values of defect of focus ε (nm) such that $\varepsilon \cdot H$ is constant. Results of the two calculations match only when both ε and H are sufficiently small.

in the *n*-PCD image. The $R^* = 6\cdot8$ images [Fig. 4(*d*)] are very like those at $R^* = 5\cdot6$.

The high-resolution $(R^* = 8\cdot0)$ *n*-beam image at $H = 5$ nm is similar to the *n*-PCD image [Fig. 4(*e*)] except that both the white and black dots are more clearly defined in the *n*-beam image. At $H = 10$ nm, white dots appear in patterns of 2×3 and 3×3 in positions corresponding to tunnels in the structure, but contrast in the positions corresponding to the overlapping octahedra is light instead of dark.

4.2.3 *Defect of focus*

Equation (5) predicts that small changes in the value of ε will merely increase or decrease the overall image contrast so long as ε remains small. At large values of ε, i.e. $|\varepsilon| > d_R^2/\lambda$, the character of the image will change. The three $W_4Nb_{26}O_{77}$ *n*-beam lattice images of Fig. 4(*a*), calculated for the same $\varepsilon.H$ as the *n*-PCD image at $R^* = 2\cdot9$, have values of $|\varepsilon|$ greater than d_R^2/λ. This leads to breakdown of the *n*-PCD approximation so that the *n*-PCD and *n*-beam images

Table 2. *Allowable defocus in n-PCD images of* $W_4Nb_{26}O_{77}$

Aperture radius R^*	Resolution d_R (nm)	d_R^2/λ (nm)	Negative defocus (nm) for maximum contrast at crystal thickness H. [Equation (5)]		
			$H = 5$ nm	$H = 10$ nm	$H = 15$ nm
2·9	0·90	220	900	450	300
4·3	0·61	100	83	42	28
5·6	0·46	60	19	10	6
6·8	0·38	40	18	9	6
8·0	0·33	30	4	2	1·3

(a)
$R^* = 2.9$
$d_R = 0.9$
$n = 15$
$\varepsilon = -900$ $\varepsilon = -300$ $\varepsilon = -150$ $\varepsilon = -100$

(b)
$R^* = 2.9$
$d_R = 0.9$
$n = 15$
$\varepsilon = -900$ $\varepsilon = -100$ $\varepsilon = -50$ $\varepsilon = -33$

(c)
$R^* = 4.3$
$d_R = 0.61$
$n = 35$
$\varepsilon = -83$ $\varepsilon = -42$ $\varepsilon = -21$ $\varepsilon = -14$

n-PCD Image   H = 5   H = 10   H = 15
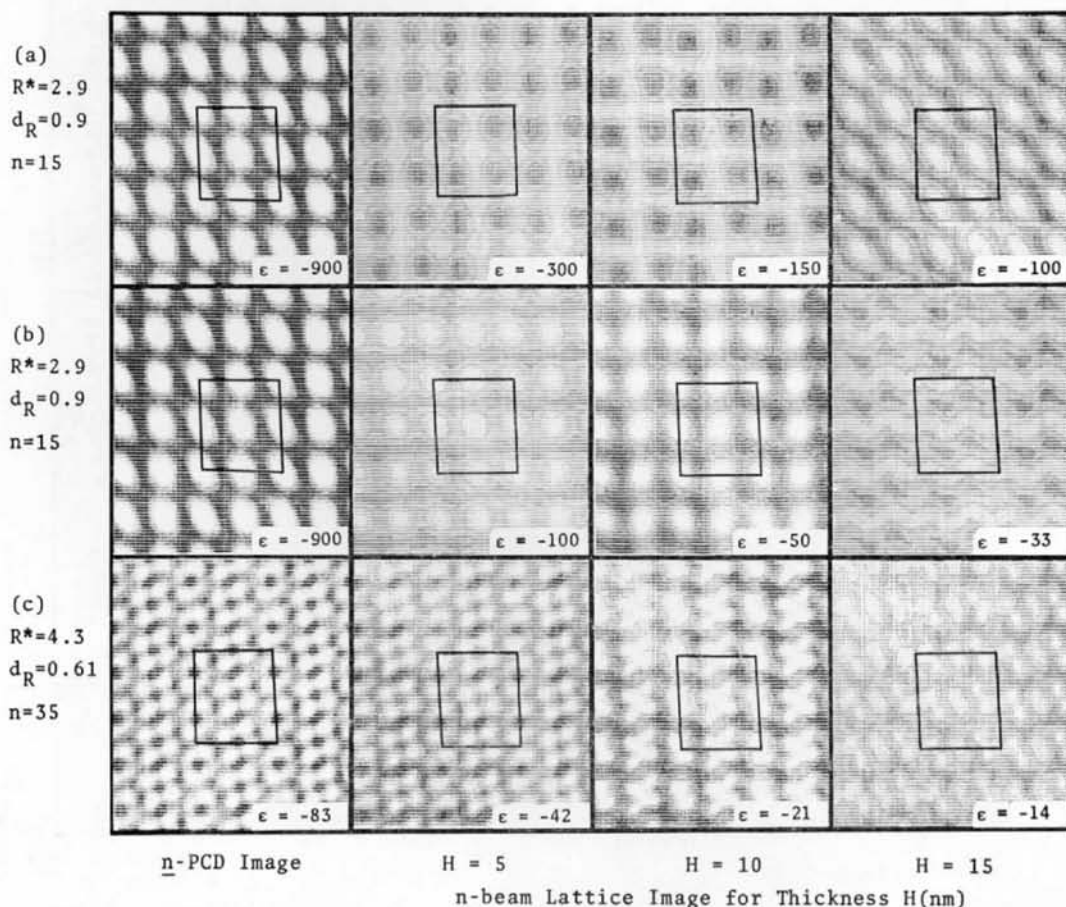
n-beam Lattice Image for Thickness H(nm)

Fig. 5. Comparison of $W_4Nb_{26}O_{77}$ *n*-PCD images (left column) with *n*-beam lattice images (remaining three columns) calculated for smaller values of ε than for Fig. 4 at resolutions of 0·9 and 0·6 nm. When ε is sufficiently small the *n*-PCD and *n*-beam images are similar in appearance although contrast in the latter is lower.

do not match. The image at $H = 10$ nm has a defocus of $\varepsilon = -450$ nm and appears as a *displaced* replica of the n-PCD image since ε is approximately half the Fourier-image-plane distance of $2d^2/\lambda$ (Cowley & Moodie, 1960) for d spacings corresponding to the strong 002 and 200 beams, and defocus by this half-distance produces a contrast reversal in the image.

Images calculated at $R^* = 2 \cdot 9$ with the value of $\varepsilon.H$ reduced to one third that of the n-PCD image showed less mismatching [Fig. 5(a)], in that the lighter areas were in the positions of the white spots of the n-PCD image. The image at $H = 10$ nm, and $\varepsilon = -150$ nm is a contrast reversal of the $H = 10$ nm, $\varepsilon = -450$ nm image [Fig. 4(a)]. A further reduction in $\varepsilon.H$, to one ninth that of the n-PCD image, produced n-PCD-like n-beam images at $H = 5$ nm and 10 nm [Fig. 5(b)] although the contrast is reduced. The images at $H = 15$ nm at no stage match the n-PCD image.

A similar result was obtained when the $R^* = 4 \cdot 3$ n-beam images of Fig. 4(b) were recalculated with the $\varepsilon.H$ value reduced to one half [Fig. 5(c)]. The $H = 5$ nm image is a good match with the n-PCD image, while at $H = 10$ nm the black dots are missing from the centres of the white regions.

Thus, the failure with increasing crystal thickness of the n-PCD approximation varies with resolution. In

t

$W_4Nb_{26}O_{77}$, the $R^* = 2 \cdot 9$ n-beam image fails to match the n-PCD image when the value of H has increased to somewhere between 10 and 15 nm [Fig. 5(b)], at $R^* = 4 \cdot 3$ for H somewhere between 5 and 10 nm [Fig. 5(c)], at $R^* = 5 \cdot 6$, $6 \cdot 8$ for $H > 5$ nm [Fig. 4(c), (d)] and in the $R^* = 8 \cdot 0$ image at $H \simeq 5$ nm [Fig. 4(e)].

4.2.4 *Spherical aberration*

Since for zero crystal tilt the phase change of a diffracted beam due to spherical aberration is proportional to the fourth power of its Bragg angle (part II), the effects of spherical aberration on the image will increase as the aperture size is increased. For values of the spherical aberration coefficient, C_s, up to 3 mm, images calculated for the two lower resolutions ($d_R \simeq 0 \cdot 9$, $0 \cdot 6$ nm) showed little change. When the aperture size was increased so that the strong beams (*e.g.*, the 601 and $\overline{2}04$ in $TiNb_{24}O_{62}$) which lie just inside the sublattice reflexions (*i.e.* the 801 and $\overline{2}06$ reflexions in $TiNb_{24}O_{62}$) were included in the image of a thin crystal, the major effects of the spherical aberration could be compensated for by decreasing ε.

This compensation of spherical aberration by defect of focus is displayed in Fig. 6 for a 5 nm thick crystal of $TiNb_{24}O_{62}$ imaged with an aperture of $R^* = 4 \cdot 5$. Fig. 6(a) shows the variation in image contrast for $C_s = 0$ with steps
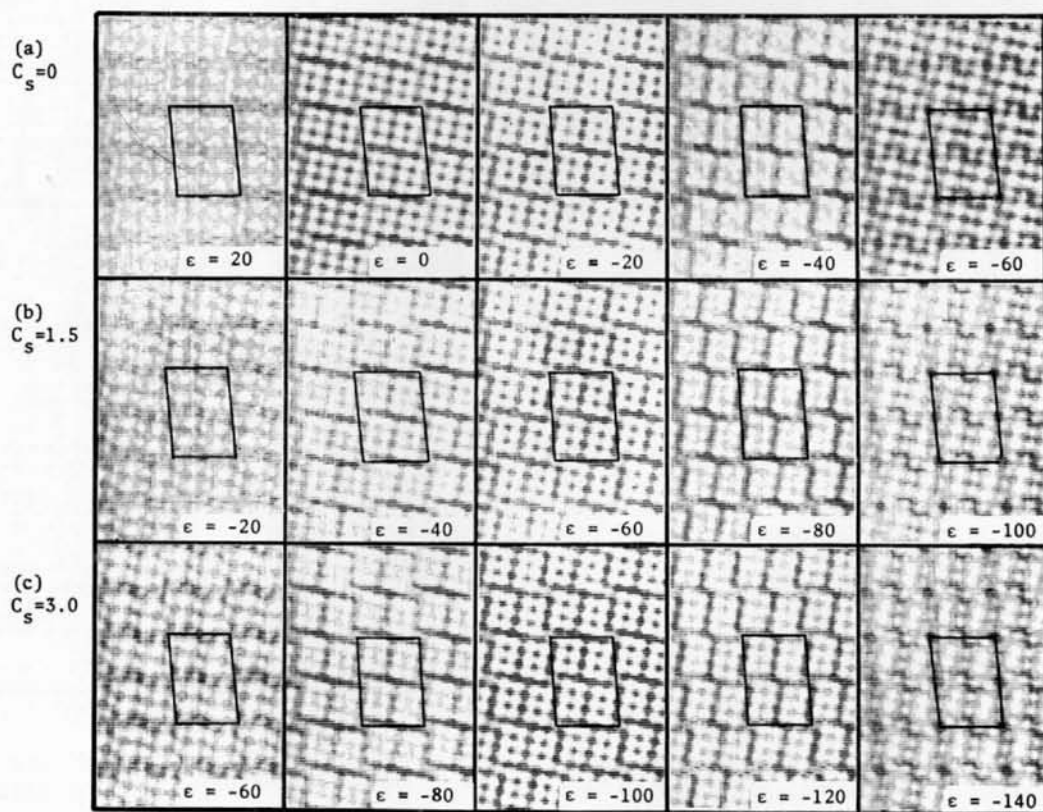

Fig. 6. n-beam lattice images for a crystal of $TiNb_{24}O_{62}$, 5 nm thick, at resolution $d_R = 0 \cdot 47$ nm ($R^* = 4 \cdot 5$), showing that increasing spherical aberration (C_s mm) can be compensated for by increasing negative defocus (ε nm).

in ε of 20 nm. The $\varepsilon = -20$ nm image matches the equivalent n-PCD image [Fig. 3(c)] quite well except that the white dots at the positions of the tetrahedral sites are less prominent. As the value of C_s is increased, these white dots become even less prominent [Fig. 6(b), $\varepsilon = -60$ nm and Fig. 6(c), $\varepsilon = -100$ nm images] while the groups of 2×3 white dots corresponding to empty tunnels remain constant in intensity.

Some features of the $C_s = 0$, $\varepsilon = -60$ nm image [Fig. 6(a)] show inverted contrast with respect to the n-PCD-like image ($\varepsilon = -20$ nm); in particular, the tetrahedral positions appear black. This can be seen more clearly in the aberrated images [Fig. 6(b), $\varepsilon = -100$ nm and Fig. 6(c), $\varepsilon = -140$ nm] where these positions appear as enhanced black dots.

Equation (2) states that the overfocus of the (h, l)th beam due to spherical aberration is $-\lambda C_s \zeta(h, l)$. For the TiNb$_{24}$O$_{62}$ 601 and $\overline{2}$04 reflexions, the values of this product at $C_s = 1.5$ mm are 43 and 44 nm overfocus respectively. These reflexions are by far the strongest (of those allowed through an aperture of $R^* = 4.5$) at a crystal thickness of $H \simeq 8$ nm [Figs. 2 and 10(a)] so that an underfocus of approximately 43 nm compensates for the effect on them of spherical aberration. The inner (weaker) reflexions require much lower degrees of underfocus and this reduces the overall defocus requirement to approximately 40 nm underfocus. Since such a defocus does not compensate fully for the spherical aberration, the images exhibit changes as C_s is increased.

4.2.5 Objective-aperture displacement

The effects of small lateral displacements of the aperture are readily investigated using the imaging calculation. If an aperture of a size such that the sublattice reflexions are just excluded was displaced so that one of these contributed to the image (a shift of 0·8 h00 units for $R^* = 5.5$ and Ti$_2$Nb$_{10}$O$_{29}$) the effects shown in Fig. 7 were obtained. At $\varepsilon = -60$ nm [Fig. 7(a)] the displaced-aperture image shows assymmetry in the direction of the a axis, the centre pair of white spots in each 2×3 group moving closer to the pair which has become larger. Interestingly, the major part of this assymmetry can be removed by increasing the negative defocus to $\varepsilon = -80$ nm [Fig. 7(b)]. Any experimental micrograph taken under these conditions would, however, be difficult to interpret in terms of the crystal structure, because of the diffuse character of the centre pair of white spots.

4.2.6 Other aberrations

Fig. 6 shows that a depth of focus of 40 nm (equivalent to averaging over the three centre images in any row) would not introduce any serious modifications to this type of image (where $R^* = 4.5$ and $H = 5$ nm). Similarly, if C_s is small so that the optimum ε is small, the blurring effect of beam divergence will be small, since this is proportional to $|\varepsilon|$. Using the measured divergence of the JEM 100B electron microscope (part II),

it was found that each point of the calculated images is enlarged to a disc of diameter 0·1 nm (i.e., approximately $\frac{1}{20}$th of the c axis) for a defocus of approximately 150 nm.

4.2.7 Summary of images near n-PCD conditions

The above results lead to the following points:

(1) n-Beam lattice images display the truncated projected charge density (n-PCD) of the structure under the conditions of H small and ε small and negative.

(2) Low-resolution images near n-PCD conditions [e.g., Fig. 3(b)] may lead to a misleading interpretation of the structure unless n-beam (or at least n-PCD) calculations are carried out.

(3) The defocus condition at which n-beam images correspond to n-PCD images, $|\varepsilon| \ll d_R^2/\lambda$, may be rewritten to a fair approximation as $|\varepsilon| < \frac{1}{2} d_R^2/\lambda$.

(4) As crystal thickness increases ($H > 5$ nm in these structures) the n-PCD approximation to the n-beam lattice image fails increasingly, and this failure occurs sooner for higher resolutions.

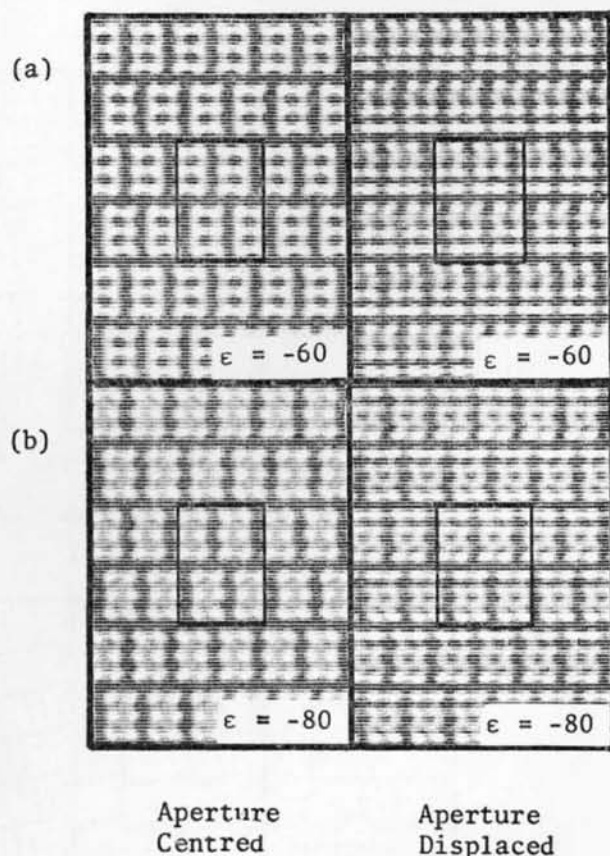(5) For a thin crystal, the 'optimum' defect of focus (i.e. the defect of focus at which the n-beam image

(a)

(b)

$\varepsilon = -60$ $\varepsilon = -60$

$\varepsilon = -80$ $\varepsilon = -80$

Aperture   Aperture
Centred   Displaced

Fig. 7. n-beam lattice images for a crystal of Ti$_2$Nb$_{10}$O$_{29}$, 5nm thick, at a resolution $d_R = 0.37$ nm ($R^* = 5.5$), showing the effects of displacing the aperture 0·8 h00 units from centre.

bears the most resemblance to the n-PCD image) depends on the crystal thickness (Fig. 8), the aperture size or number of beams contributing to the image (Figs. 4, 5) and on the magnitude of the spherical aberration (Fig. 6), as well as on the crystal structure.

(6) Where the strongest beams contributing to the lattice image all lie at approximately the same Bragg angle, and other contributing reflexions are weak, spherical aberration may, to some degree, be compensated for by additional underfocus (Fig. 6).

(7) In this class of compounds, the inclusion of those beams just inside the sublattice reflexions is necessary in order to resolve the vacant tunnels in the structure.

4.3 Images outside n-PCD conditions

The dependence of the $Ti_2Nb_{10}O_{29}$ n-beam image on ε and H is shown in Fig. 8 for $R^* = 4\cdot5$ and $C_s = 1\cdot5$ mm.

As in the case of $W_4Nb_{26}O_{77}$ [Fig. 4(c)], the departure from the n-PCD image [Fig. 3(c)] increases with increasing crystal thickness. The Figure also illustrates the requirement of equation (5), that for the n-beam image to remain like the n-PCD approximation, an increase in H must be accompanied by a decrease in $|\varepsilon|$. At $H = 4$ nm, the image most like the n-PCD image [Fig. 3(c)] is that at $\varepsilon = -60$ nm. This becomes approximately $\varepsilon = -50$ nm at $H = 6$ nm while at $H = 8$ nm it is approximately $\varepsilon = -30$ nm. Although by $H = 10$ nm
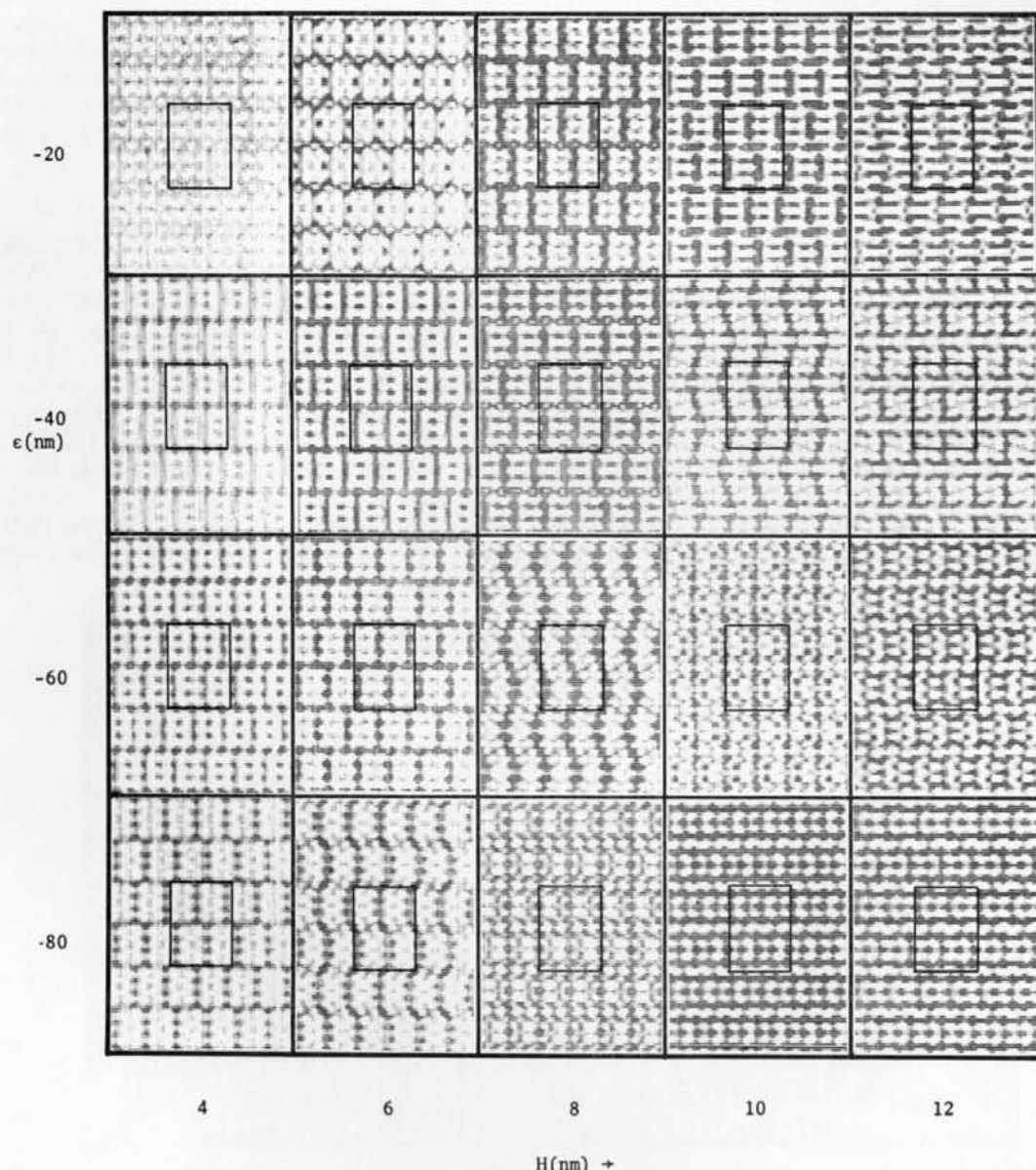

Fig. 8. $Ti_2Nb_{10}O_{29}$ n-beam lattice images ($n = 39$) calculated for an 00l aperture radius, $R^* = 4\cdot5$, and a spherical-aberration coefficient, $C_s = 1\cdot5$ mm. The Figure shows the variation in image contrast with crystal thickness, H (nm), and defect of focus, ε (nm).

the *n*-beam image differs quite markedly from the *n*-PCD image, a comparison of these two shows that the positions of the blocks of octahedra could be obtained in a experimental micrograph from a crystal of this thickness.

4.3.1 *Large values of defocus*

Fourier image theory (Cowley & Moodie, 1957*b*) predicts that images containing major periodicities of *d* will tend to repeat at intervals in ε of $2d^2/\lambda$. For image detail corresponding to the strong 600 and 004 reflexions in $Ti_2Nb_{10}O_{29}$, the values of this term become 122 and 142 nm respectively. Detail in the recurrent images will be modified by the weak beams also allowed through the aperture, but the effect can be seen when spherical aberration is present.

The $\varepsilon = -60$ nm image of Fig. 9 is at the optimum defocus (at $H = 5$ nm and $C_s = 1\cdot8$ mm) to display the $Ti_2Nb_{10}O_{29}$ structure. The $\varepsilon = -200$ nm image shows many of the characteristics of the optimum image, its major defect being that the centre pair of white spots in each group of 2×3 is over-emphasized while the other pairs are too faint.

The images formed at values of defocus midway between Fourier image planes tend to show contrast reversal with respect to images on these planes. The $\varepsilon = -120$ nm image, with strong white spots at the positions of the two MO_6 octahedra that lie inside each 2×3 group of tunnels, is an approximate contrast reversal of the optimum image. These interior octahedra appear white in the $\varepsilon = -20$ nm image, become grey at $\varepsilon = -40$ nm, black at $\varepsilon = -60$ nm, fade to grey at $\varepsilon = -80$ nm and appear white in the $\varepsilon = -100$ nm image. The same sequence is followed by the interior octahedra in $TiNb_{24}O_{62}$ [Fig. 6(*b*)].

It should be remembered that any divergence of the incident electron beam (part II) will mask these effects in experimental images at large values of $|\varepsilon|$.

4.3.2 *Crystal thickness*

Examination of plots of the calculated diffracted beam intensities, $I(h0l)$, against crystal thickness, H, (Fig. 2) indicated that the $h0l$ diffraction pattern should show a quasiperiod (part III) of approximately 17 nm; calculated diffraction patterns confirmed this. In Fig. 10(*a*), each reflexion is displayed as a disc of the approximate size of the discs found when an experimental diffraction pattern is taken under imaging conditions in a JEM 100B electron microscope (parts I and II). The pattern that occurred for $H = 8$ nm was approximately repeated when the 000 beam reached minima at $H = 42$, 58 and 76 nm. Images calculated at these crystal thicknesses [Fig. 10(*b*)] showed more resemblance to that at $H = 8$ nm than ones calculated for arbitrary thickness (*e.g.*, $H = 50$ nm) but no longer display the structure of the crystal.

4.3.3 *Crystal tilt*

In parts I, II and III of this series of publications, images were calculated for crystals of $W_4Nb_{26}O_{77}$ tilted about the c^* axis by $0\cdot1$ rad (*i.e.* into an approximate 00*l* systematics orientation). Since most of the electron energy remained in the 00*l* set of reflexions, only these were considered in the (one-dimensional) inverse Fourier summation carried out to produce the image. However, some electron energy was present in the off-systematics reflexions (notably the 200 and 205 reflexions) allowed through the aperture. Two-dimensional image calculations which include all beams passing through the aperture have now been
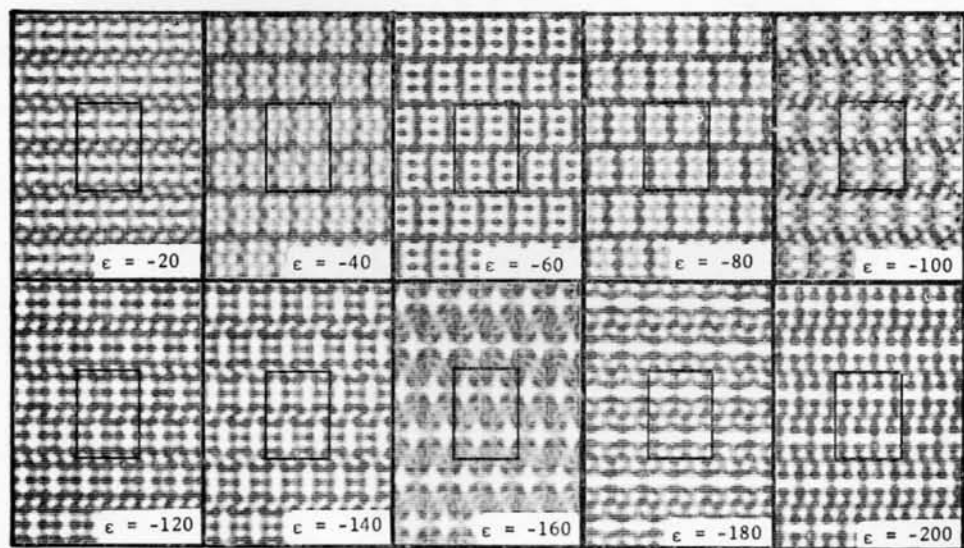

Fig. 9. $Ti_2Nb_{10}O_{29}$ *n*-beam images calculated for $R^* = 5\cdot5$ ($n = 59$), $H = 5$ nm and $C_s = 1\cdot8$ mm. Values of defocus, ε (nm), are indicated. The images at $\varepsilon = -40$ nm and $\varepsilon = -200$ nm are similar, and the intermediate image at $\varepsilon = -120$ nm shows inverted contrast.

carried out for comparison with the earlier one-dimensional ones.

Images calculated for a crystal of $W_4Nb_{26}O_{77}$ of thickness, $H = 30$ nm, using an aperture of radius $R^* = 5.5$ are shown in Fig. 11 for both the two-dimensional (*a*) and one-dimensional (*b*) *n*-beam image cal-

culations. The differences are not marked except for the image at $\varepsilon = -20$ nm, which is close to one-dimensional *n*-PCD conditions (part II). At this defocus, the two-dimensional calculation shows quite strong modulation along the fringes; however, this modulation is due to features only $0.2-0.3$ nm across, so that
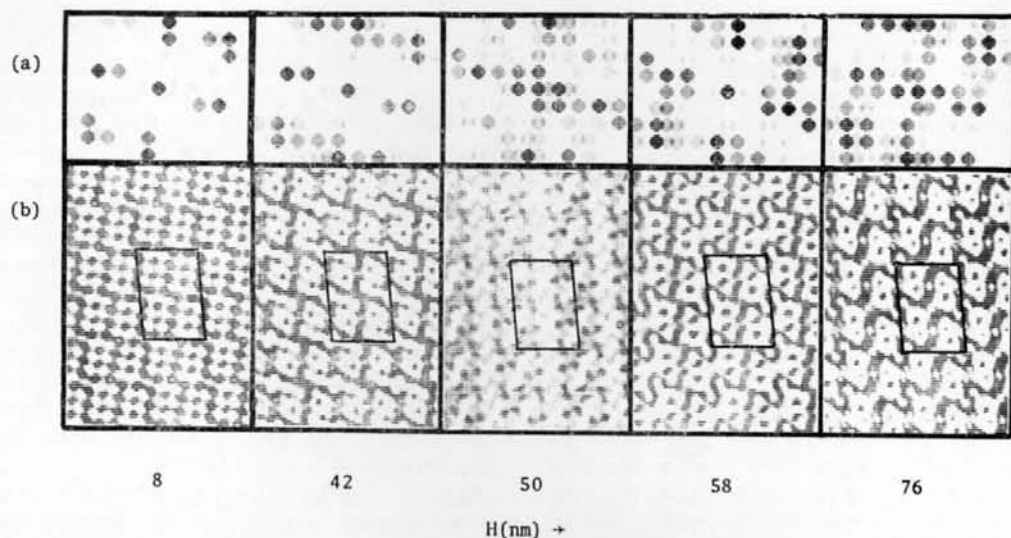

Fig. 10. Calculated *h0l* diffraction pattern (*a*) and *n*-beam ($n = 47$) lattice image (*b*) for $TiNb_{24}O_{62}$ for five values of crystal thickness, H (nm). The diffraction pattern shows the more intense spots as darker discs of diameter appropriate to the JEM100B electron microscope used under the conditions of part I. The lattice images were calculated for a defect of focus, $\varepsilon = -40$ nm and a spherical-aberration coefficient, $C_s = 1.5$ mm. Images at values of H of 42, 58 and 76 nm show more similarity to that at $H = 8$ nm than images calculated at arbitrary thicknesses.
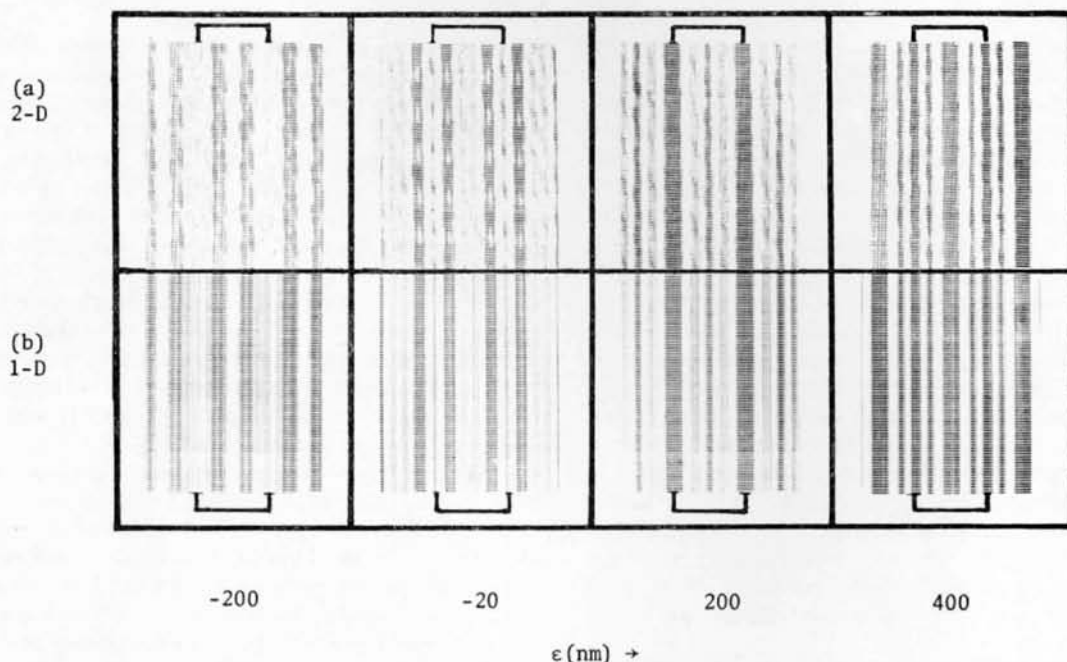

Fig. 11. Images calculated using (*a*) the two-dimensional image calculation, and (*b*) the one-dimensional approximation. The input to these calculations consisted of the diffracted beam amplitudes and phases from a (two-dimensional) 435-beam multislice calculation for a 30 nm thick crystal of $W_4Nb_{26}O_{77}$ tilted 0.1 rad about the c^* axis. The aperture radius used for imaging was $R^* = 5.6$ giving (*a*) $n = 59$ *h0l* beams and (*b*) $n = 11$ *00l* beams. One unit cell repeat distance in the c direction is marked.

it was not resolved in the aberrated experimental micrographs of part I.

Thus, for crystals viewed in a systematics orientation, the one-dimensional approximation to the *n*-beam image calculation can provide quite a valid picture of the image even if non-systematics reflexions contributing to the image have intensities large enough to be seen in the diffraction pattern. This is extremely useful, as the one-dimensional (systematics) *n*-PCD approximation holds to much greater crystal thicknesses than the two-dimensional case, *e.g.*, it is applicable up to approximately 30 nm for $W_4Nb_{26}O_{77}$ in the 00*l* systematics orientation (part II).

5. Discussion

The experimental many-beam lattice images reported by various authors may be examined in the light of the above results. These reported images were often photographed at small negative defects of focus to suit Scherzer's (1949) condition of optimum defocus in order to enable interpretation in terms of amplitude contrast. The 'optimum-defocus condition' attempts to balance the phase changes introduced by defocus and spherical aberration, but not those due to dynamical scattering within the specimen, although kinematical scattering is included in the treatment of Eisenhandler & Siegel (1966). Dynamical phase changes may be quite large, even in the systematics case, as shown in parts I and II. The *n*-PCD approximation, based on the 'thin-phase-grating' approximation takes such dynamical effects into consideration, and predicts that small negative defects of focus will produce images of the *n*-coefficient projected charge density in the crystal, the image contrast being proportional to the defect of focus, ε. Since the *n*-PCD series is truncated by the aperture, unexpected features may occur in the image such as the black spots on the central tunnel positions of the 4×4 groups of octahedra in $W_4Nb_{26}O_{77}$ at a resolution of 0·6 nm [Fig. 3(*b*)] and the white dots at tetrahedral sites in $W_4Nb_{26}O_{77}$ and $TiNb_{24}O_{62}$ at resolutions of approximately 0·4 nm [Fig. 3(*c*), (*d*)]. These white dots occur even when spherical aberration is included [Fig. 6(*b*), (*c*)] and when *H* becomes too large to fully satisfy the thin-phase-grating approximation [*e.g.*, $H = 8$ nm in Fig. 10(*b*)], and may be seen in experimental micrographs of sufficiently thin crystals of $TiNb_{24}O_{62}$ (Iijima, private communication).

Such a truncation effect apparently occurs also in the Cu-hexadecachlorophthalocyanine *n*-beam lattice image published by Uyeda, Kobayashi, Suito, Harada & Watanabe (1970) which shows the shapes of the molecules as black quatre-foils, but with white spots at the centres, *i.e.* at positions corresponding to the heavy Cu atoms.

Equation (5) predicts that in *n*-beam images close to *n*-PCD conditions, the image contrast at $+\varepsilon$ will be the inverse of that at $-\varepsilon$. However, the effect of spherical aberration is to bias the defect of focus of

each reflexion by $-\lambda C_s \zeta(h, l)$, so that image features which result from the various diffracted beams will show antisymmetric contrast about various negative defects of focus instead of about $\varepsilon = 0$. Images of $19Nb_2O_5 . 63WO_3$. published by Cowley & Iijima (1972*a*) show contrast reversal of the coarser detail between micrographs obtained with $\varepsilon = +30$ nm and $\varepsilon = -90$ nm, indicating a mean bias of $\varepsilon = -30$ nm due to spherical aberration.

Calculations of *H*-Nb_2O_5 image contrast carried out by Hewat (1970) using the thin-phase-grating approximation and a resolution $d_R = 0·65$ nm, predicted an image composed of a white spot centred on each block of octahedra and black lines at positions of block overlap in the manner of the 0·9 nm resolution *n*-PCD image of $W_4Nb_{26}O_{77}$ [Fig. 3(*a*)]. The *N*-Nb_2O_5 bright-field image by Hutchison & Anderson (1972), obtained at a nominal resolution of 0·5 nm and an unspecified negative defect of focus, shows white spots bordered by black lines. However, the possibility exists that the defect of focus may have been sufficiently large to produce the effect shown in the *n*-beam images of Fig. 4(*b*) with a crystal thickness lying between $H = 5$ and 10 nm.

Allpress (1969*b*, 1970) has obtained experimental many-beam lattice images of similar oxides at resolutions of approximately 0·8 nm, and from these has identified black dots in underfocused images with tetrahedral positions. Similar black dots appear at tetrahedral sites in *n*-beam images of $TiNb_{24}O_{62}$ calculated for an aperture of $R^* = 4·5$ ($d_R = 0·5$ nm) when ε is more negative than is required to satisfy *n*-PCD conditions [Fig. 6(*c*), $\varepsilon = -140$ nm].

Comparison of a series of micrographs obtained using different defects of focus (through-focus series) with equivalent computed images offers the best test of the assumed crystal structure (and of the calculations). The experimental images of $Ti_2Nb_{10}O_{29}$ published by Cowley & Iijima (1972*b*) taken at nominal defects of focus of $\varepsilon = -160$ nm and -96 nm appear to be slightly blurred replicas of the images calculated for $\varepsilon = -120$ nm and -60 nm (Fig. 9). The blurred effect is probably due to beam divergence, while differences in detail may be due to the effect of chromatic aberration (depth-of-focus). The discrepancy in values of ε may be due to a difference between the experimental values of C_s and *H* and those used in calculating the images of Fig. 9.

A possible danger in interpretation of experimental micrographs imaged at resolutions of approximately 0·4 nm is that of interpreting thicker areas of crystal as different structures. This could arise at a surface step, *e.g.*, an abrupt change from $H = 8$ nm to $H = 10$ nm in a crystal of $Ti_2Nb_{10}O_{29}$ imaged at $R^* = 4·5$ and $\varepsilon = -40$ nm would produce the changes shown in Fig. 8.

assistance provided by the members of the Electron Diffraction Section, in particular Mr A. F. Moodie and Dr D. F. Lynch. Many thanks are due to Mr J. G. Allpress and Dr J. V. Sanders for their helpful discussions and for critical reading of the manuscript.

References

ALLPRESS, J. G. (1969a). J. Solid State Chem. 1, 66–81.
ALLPRESS, J. G. (1969b). Mater. Res. Bull. 4, 707–720.
ALLPRESS, J. G. (1970). J. Solid State Chem. 2, 78–93.
ALLPRESS, J. G., HEWAT, E. A., MOODIE, A. F. & SANDERS, J. V. (1972). Acta Cryst. A28, 528–536.
ALLPRESS, J. G., SANDERS, J. V. & WADSLEY, A. D. (1969). Acta Cryst. B25, 1156–1164.
ANDERSON, J. S., BROWNE, J. M. & HUTCHINSON, J. L. (1972a). Nature, Lond. 237, 151–153.
ANDERSON, J. S., BROWNE, J. M. & HUTCHINSON, J. L. (1972b). J. Solid State Chem. 5, 419–431.
ANDERSSON, S., MUMME, W. G. & WADSLEY, A. D. (1966). Acta Cryst. 21, 802–808.
ANSTIS, G. R., LYNCH, D. F., MOODIE, A. F. & O'KEEFE, M. A. (1973). Acta Cryst. A29, 138–147.
COWLEY, J. M. & IIJIMA, S. (1972a). Proc. 30th Ann. Electron Microsc. Soc. Amer. Edited by C. J. ARCENEAUX, pp. 550–551.
COWLEY, J. M. & IIJIMA, S. (1972b). Z. Naturforsch. 27a, 445–451.

COWLEY, J. M. & MOODIE, A. F. (1957a). Acta Cryst. 10, 609–619.
COWLEY, J. M. & MOODIE, A. F. (1957b). Proc. Phys. Soc. B70, 486–496.
COWLEY, J. M. & MOODIE, A. F. (1960). Proc. Phys. Soc. 76, 378–384.
COWLEY, J. M. & MOODIE, A. F. (1962), J. Phys. Soc. Japan, Suppl. B-II, 17, 86–91.
EISENHANDLER, C. B. & SIEGEL, B. M. (1966). J. Appl. Phys. 37, 1613–1620.
HEAD, A. K. (1967). Aust. J. Phys. 20, 557–566.
HEWAT (née CHIDZEY), E. A. (1970). M. Sc. Thesis, Univ. of Melbourne.
HUTCHINSON, J. L. & ANDERSON, J. S. (1972). Phys. Stat. Sol. (a) 9, 207–213.
IIJIMA, S. (1971). J. Appl. Phys. 42, 5891–5893.
IIJIMA, S. (1973). Acta Cryst. A29, 18–24.
IIJIMA, S. & O'KEEFE, M. A. (1973). In preparation.
LYNCH, D. F. & O'KEEFE, M. A. (1972). Acta Cryst. A28, 536–548.
MOODIE, A. F. (1973). To be published.
ROTH, R. S. & WADSLEY, A. D. (1965). Acta Cryst. 18, 724–730.
SCHERZER, O. (1949). J. Appl. Phys. 20, 20–29.
UYEDA, N., KOBAYASHI, T., SUITO, F., HARADA, Y. & WATANABE, M. (1970). Microsc. Electron. 1, 23–24.
VAN LANDUYT, J., VOCHTEN, R. & AMELINCKX, S. (1970). Mater. Res. Bull. 5, 275–280.
WADSLEY, A. D. (1961). Acta Cryst. 14, 664–670.

Exponential Form of Joint Probability Distribution; Unequal Atoms

BY J. KARLE AND R. D. GILARDI

Laboratory for the Structure of Matter, Naval Research Laboratory, Washington D.C. 20375, U.S.A.

The joint probability distributions for three structure factors whose subscripts add to zero, in the general case of unequal atoms, are expressed in an exponential form for space groups $P1$ and $P\bar{1}$. The latter are representative of noncentrosymmetric and centrosymmetric space groups respectively. The exponential form possesses considerably improved convergence properties over those of the standard asymptotic series, although it too remains asymptotic. With the range of values ordinarily obtained for the normalized structure-factor magnitudes, the exponential forms are quite accurate. However, the accuracy deteriorates somewhat as these magnitudes approach their largest possible values. By altering the exponential form with the use of a result from the inequality theory, joint probability distributions are obtained which are accurate over the entire range of values for the structure-factor magnitudes and are most accurate at the largest values. Several probability measures of interest are derived from the joint distribution functions such as expected values, variances and the probability that a structure factor has a positive sign. Numerical tests indicate that the derived probability measures are very reliable and that their validity extends to higher space groups than $P1$ and $P\bar{1}$.

Introduction

The exponential form of the joint probability distribution for three structure factors ($h_1 + h_2 + h_3 = 0$) in the equal-atom case has been derived for space groups $P1$ and $P\bar{1}$ (Karle, 1972). The virtue of this form is the considerably improved convergence properties of the ex-

ponential series over those for the ordinary series expansion (Bertaut 1960a, b; Karle, 1972). It is of interest to consider whether exponential series possessing the improved convergence properties can be obtained for the joint probability distributions in the case of unequal atoms. It is found that this is the case and, as occurs for equal atoms, terms of the order $N^{-m/2}$ in the exponen-